INSILI 1 (2025) 100099

Contents lists available at ScienceDirect

In Silico Research in Biomedicine

journal homepage: www.sciencedirect.com/journal/in-silico-research-in-biomedicine

Targeting the untargetable: accelerated discovery of KRAS G12D inhibitors through a deep learning-enhanced in silico pipeline

Elisabetta Grazia Tomarchio [a,b], Chiara Zagni [a], Antonio Rescifina [a,*]

[a] Department of Drug and Health Sciences, University of Catania, V.le A. Doria 6 95125, Catania, Italy
[b] Department of Biomedical and Biotechnological Sciences, University of Catania, Via Santa Sofia 97 95123, Catania, Italy

ARTICLE INFO

Keywords:
KRAS G12D
Virtual screening
Drug repurposing
Molecular docking
GNINA
CNN affinity
Molecular dynamics
Machine learning

ABSTRACT

KRAS mutations represent some of the most prevalent oncogenic alterations in human cancers, especially in pancreatic, colorectal, and non-small cell lung carcinomas. Among these, the KRAS G12D mutation is notably aggressive, producing a constitutively active KRAS protein that drives unchecked cell proliferation and therapeutic resistance. Developing effective inhibitors against this mutation remains a significant challenge and a critical objective in precision oncology. Traditional drug discovery approaches, while valuable, are often time-intensive and financially demanding. In this context, computational drug repurposing offers a strategic advantage by accelerating the identification of novel therapeutic applications for FDA-approved drugs with established safety profiles. This study presents a robust, integrated in silico workflow designed to screen FDA-approved compounds and commercial libraries for potential inhibitors of the KRAS G12D mutation. The pipeline combines pharmacophore-based filtering, GNINA deep learning-augmented molecular docking, and molecular dynamics (MD) simulations to prioritize candidates with strong binding affinity and structural stability. Application of this multi-tiered approach yielded three high-confidence compounds exhibiting favorable and persistent interactions within the KRAS G12D switch-II pocket. These findings lay the groundwork for subsequent experimental validation and provide a promising avenue for the rapid development of therapeutic interventions against KRAS-driven cancers.

1. Introduction

Mutations in KRAS (Kirsten rat sarcoma viral oncogene homolog) represent a cornerstone of oncogenic signaling in multiple malignancies, notably pancreatic ductal adenocarcinoma (PDAC), non-small cell lung cancer (NSCLC), and colorectal cancer (CRC) [1]. Among these, the KRAS G12D substitution, which replaces glycine with aspartic acid at codon 12, is one of the most prevalent and therapeutically challenging mutations, implicated in driving aggressive tumor phenotypes and poor clinical outcomes [2]. Efforts to directly target KRAS G12D have long faced significant challenges, to the extent that the protein has earned the reputation of being "undruggable" [3,4]. The mutation stabilizes the protein in its active, GTP-bound conformation, which, coupled with the exceptionally high affinity of KRAS for GTP/GDP and the absence of accessible druggable pockets, has thwarted traditional small-molecule inhibitor development [5,6]. While covalent inhibitors against KRAS G12C, such as sotorasib and adagrasib, have marked a breakthrough in RAS-targeted therapy [7,8], KRAS G12D lacks the reactive cysteine required for analogous covalent engagement, necessitating alternative strategies. Drug repurposing has emerged as a powerful approach to circumvent the bottleneck in de novo drug development. By exploiting the extensive landscape of FDA-approved drugs with well-characterized pharmacological properties, repurposing efforts aim to rapidly identify candidate molecules capable of modulating KRAS function [9–11]. This strategy has proven particularly successful in the field of oncology, with several notable examples of drug repurposing. Thalidomide, initially developed as a treatment for morning sickness, was later repurposed for multiple myeloma due to its immunomodulatory effect [12]. Similarly, tretinoin, commonly used as a topical treatment for acne, found a new application in the treatment of acute promyelocytic leukemia by targeting the PML-RARα pathway [13]. Another example is raloxifene, originally used to treat osteoporosis, which has been repurposed for breast cancer prevention through its selective modulation of estrogen receptors [14].

Complementing this approach, the evolution of high-throughput, structure-based virtual screening (HTVS) workflows has enabled more

* Corresponding author.
E-mail address: antonio.rescifina@unict.it (A. Rescifina).

https://doi.org/10.1016/j.insi.2025.100099
Received 11 July 2025; Received in revised form 10 September 2025; Accepted 9 October 2025
Available online 10 October 2025

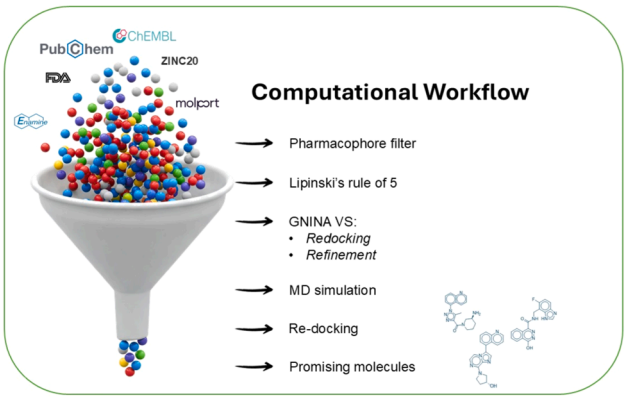

Fig. 1. Graphic representation of the computational workflow employed in this work.

systematic and expansive exploration of chemical space, particularly when coupled with advances in machine learning. These advances have significantly accelerated the early phases of drug discovery by enabling the rapid prioritization of candidate molecules from vast compound libraries, thereby reducing both time and cost compared to traditional experimental screening methods. Machine learning-enhanced docking tools, such as GNINA, are reshaping the landscape of computational drug discovery, particularly for proteins that are challenging to target, like KRAS G12D. What sets GNINA apart is its integration of convolutional neural networks (CNNs) into the docking workflow, enabling deep learning models to recognize complex interaction patterns between ligands and protein binding sites. Unlike traditional scoring functions, which rely on relatively simple physical and empirical rules, CNNs learn directly from structural data, enabling more accurate predictions of both binding poses and affinities [15,16]. Moreover, GNINA's ability to integrate diverse training datasets and adapt to various protein targets may improve its generalizability and robustness, suggesting potential usefulness in exploring challenging targets with subtle and dynamic binding pockets [15]. In recent benchmarking studies, GNINA has consistently outperformed classical approaches in pose prediction tasks, showing better correlation between predicted and experimental binding affinities [17]. These improvements make GNINA a powerful tool in modern in silico drug discovery pipelines, offering a more data-driven and accurate approach to virtual screening (VS), especially in challenging systems such as RAS proteins.

A recent breakthrough in KRAS G12D targeting is represented by MRTX1133, a potent and selective non-covalent inhibitor that binds to an induced allosteric pocket beneath the switch II region of KRAS, stabilizing its inactive GDP-bound state [18,19]. This compound has demonstrated promising preclinical efficacy, significantly inhibiting tumor growth in KRAS G12D-driven models, thus validating the allosteric pocket as a viable druggable site. Unlike KRAS G12C inhibitors, MRTX1133 achieves high affinity through precise non-covalent interactions, therefore paving a new route for pharmacophore-driven inhibitor design. However, despite these advances, challenges remain in optimizing pharmacokinetic properties and overcoming potential resistance mechanisms, underscoring the need for discovering additional chemical scaffolds. Building on these insights, the objective of the present study was to design and validate a systematic computational workflow capable of identifying novel KRAS G12D ligands (Fig. 1). Leveraging a pharmacophore model derived from the key interaction motifs of MRTX1133, an initial VS was performed to select candidate molecules. These candidates were subsequently subjected to deep learning-based docking using GNINA to refine binding pose predictions and prioritize leads. Finally, molecular dynamics (MD) simulations were employed to evaluate the dynamic stability and binding persistence of the docked complexes under physiologically relevant conditions. This integrated strategy aims to overcome traditional limitations in RAS drug discovery, offering a robust platform for the rational identification of novel therapeutic agents targeting KRAS G12D.

2. Materials and methods

2.1. Protein preparation

The protein structure was downloaded from the Protein Data Bank (https://www.rcsb.org/, accessed January 25, 2025); PDB ID: 7RPZ (KRAS G12D co-crystallized with MRTX1133) [20]. Protein was prepared for docking using YASARA (v. 19.5.5, YASARA Biosciences GmbH, Vienna, Austria) "Clean>All" command [21], which adds missing atoms, side chains, and hydrogen atoms while ensuring correct protonation states at physiological pH. Water molecules, ions, and other non-essential co-crystallized molecules were removed before docking. The prepared protein structure was then subjected to energy minimization using the YASARA macro *em_run.mcr* with the ff14SB protein force field (a subset of AMBER14 optimized for proteins). Minimization was carried out using the default settings of the macro, specifically until the energy improved by less than 0.01 kcal/mol per atom. The resulting minimized structure was saved in PDB format for subsequent docking studies.

2.2. Pharmacophore-based pre-screening

A pharmacophore model was constructed based on known binding features of KRAS inhibitor MRTX1133, using PDB entry 7RPZ. Screening was conducted using the Pharmit server (https://pharmit.csb.pitt.edu) (https://doi.org/10.1093/nar/gkw287) to identify compounds matching key features (H-bond donors/acceptors, aromatic rings, hydrophobic centers). Several Pharmit pre-built libraries were used to screen compounds. The query-aligned poses were minimized and filtered by affinity (e.g., > -7 kcal/mol) and mRMSD to eliminate poses with unfavorable binding energies and significant deviations from the original query (e.g., 2 Å). Compounds that passed these filters were downloaded as SDF files.

2.3. Filtering, clustering, and ligand preparation

Compounds filtered from all databases screened were merged into a unique database and further refined in DataWarrior (v. 06.04.01) [22]. Toxic, mutagenic, or reactive structures were removed, and then the physicochemical properties (MW, logP, TPSA, etc.) were evaluated to filter by the Lipinski rule of five. For the preparation of three-dimensional (3D) molecular structures, Open Babel (v. 3.1.1) was employed.

2.4. Molecular docking simulation

Molecular docking simulations were performed using GNINA (v. 1.3), a deep learning-enhanced docking platform derived from SMINA and based on the AutoDock Vina architecture [15,16]. Two distinct GNINA docking protocols were employed: *rescore* and *refinement*. The initial HTVS was conducted using the *rescore* mode, which enables rapid evaluation by applying 15 rotational ligand conformations per compound. From this preliminary screening, top-performing candidates were further evaluated using the more computationally intensive *refinement* mode, which increases docking accuracy by eliminating ligand pose rotations (set to zero) and allowing for finer local optimization. Both docking runs ranked ligand-protein complexes based on the CNN score, a CNN-derived metric trained to predict binding pose quality and interaction strength.

The docking grid was defined on the prepared 7RPZ protein using AutoDock Tools (v. 1.5.7), with the binding site centered on the coordinates of the co-crystallized ligand in the KRAS G12D crystal structure. Grid center coordinates were set to $x = 2.794$, $y = 5.538$, and $z = -21.918$ for the center coordinates; $x = 22$, $y = 20$, and $z = 26$ for the

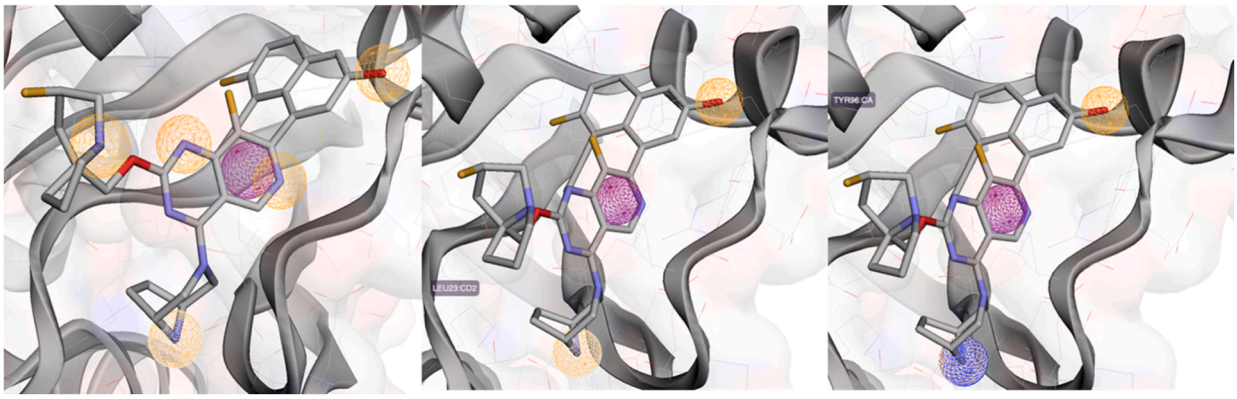

Fig. 2. Pharmit pharmacophoric models, based on MRTX1133, including hydrogen bond donors (DON) (blue spheres), hydrogen bond acceptors (ACC) (orange spheres), and the hydrophobic center (HYD) (violet spheres).

npts dimensions with a spacing of 1.00 Å.

Following MD simulations, a redocking step was performed using the GNINA refinement protocol. Grid center coordinates were updated to reflect the new center of mass of the equilibrated binding site derived from the final MD frame, allowing for more accurate pose refinement under conformationally relaxed conditions.

2.5. Decoy generation

To construct a balanced benchmarking set for virtual screening evaluation, a decoy dataset was generated using the LUDe (LIDeB's Useful Decoys) tool [31], which applies topological and physicochemical property filters to ensure unbiased decoy selection [23]. As a reference set of active compounds, the 50 most potent KRAS G12D ligands, retrieved from BindingDB based on reported binding affinities, were employed [24]. From the complete decoy pool generated by LUDe, a subset of 2000 molecules was selected to represent false positives. Both active and decoy compounds were processed according to the preparation protocol described in Section 3.2, which included protonation at physiological pH, 3D structure generation, and energy minimization to ensure consistency across the dataset.

2.6. Molecular dynamics simulation

MD simulations were performed using the YASARA Software suite with the *md_runfast.mcr* macro to achieve an optimized balance between computational efficiency and simulation accuracy. A cubic simulation box was constructed with a 5 Å buffer surrounding all protein atoms, and periodic boundary conditions were applied in all directions to mimic an infinite system. Simulations were conducted at physiological pH in a 0.9 % NaCl aqueous solution, maintaining a constant temperature of 298 K and a water density of 0.997 g/mL, approximating physiological conditions. The simulation was run using the ff14SB force field for the solute, GAFF2 force field with the AM1BCC charges for ligands, and the TIP3P scheme for water. A cut-off of 8 Å was applied for van der Waals interactions, and no cutoff was applied to electrostatic forces (using the Particle Mesh Ewald algorithm). The equations of motion were integrated with multiple time steps of 2.5 fs for bonded interactions and 5.0 fs for nonbonded interactions at a temperature of 298 K and a pressure of 1 atm. A short MD simulation was run on the solvent only to remove clashes. The entire system was then energy minimized using the steepest descent minimization to remove conformational stress, followed by a simulated annealing minimization until convergence (<0.01 kcal/mol Å). Finally, 100 ns MD simulations were conducted without restrictions, and the conformations were recorded every 200 ps. The RMSD and total internal energy were analyzed throughout the simulation using the *md_analyze.mcr* macro to assess system stability and equilibration.

To capture a representative conformation for redocking analysis, the average structure from the final 40 ns of the trajectory (from 60 to 100 ns) was computed and subsequently used for post-MD redocking studies.

2.7. Principal component analysis

Principal component analysis (PCA), a multivariate statistical technique, was employed to investigate the collective motions of protein-ligand complexes during the 100 ns MD simulations. For this purpose, a covariance matrix of backbone (N, C, and Cα) atom fluctuations was constructed and diagonalized to extract the dominant modes of motion. PCA reduces the dimensionality of complex datasets while retaining the most relevant information, thereby facilitating the identification of large-scale conformational changes that are otherwise difficult to capture.

The global dynamics of the receptor-ligand complexes were primarily assessed through the first two principal components, PC1 (projection on eigenvector 1) and PC2 (projection on eigenvector 2), which capture the most significant modes of collective motion and provide insight into the conformational flexibility and stability of the studied systems. We also used the apo form crystallographic structure of KRAS G12D retrieved from the Protein Data Bank (PDB ID 6QUU).

2.8. Visualization and reporting

All structural and trajectory analyses were performed using YASARA Software and Discovery Studio Visualizer (Dassault Systèmes BIOVIA, 2021) [32]. These tools enabled high-resolution inspection of protein-ligand complexes and facilitated the generation of 2D interaction diagrams.

3. Results and discussion

3.1. Pharmacophoric search

A pharmacophore represents a set of key molecular features and their three-dimensional arrangement that are critical for a compound to interact effectively with a specific biological target [25]. In structure-based approaches, pharmacophore models are typically derived from the 3D structure of the protein-ligand complex, allowing for the inclusion of precise spatial and interaction data. This enables the identification of regions within the binding site that are most favorable for ligand engagement, enhancing the accuracy of virtual screening and lead optimization. Among the numerous crystallographic structures of KRAS G12D available in the Protein Data Bank (PDB), the structure with PDB ID 7RPZ, co-crystallized with the inhibitor MRTX1133, was selected as the model for this computational study [18,20]. Taking MRTX1133 as the reference ligand, an initial pharmacophore-based screening was conducted using the Pharmit online platform (http

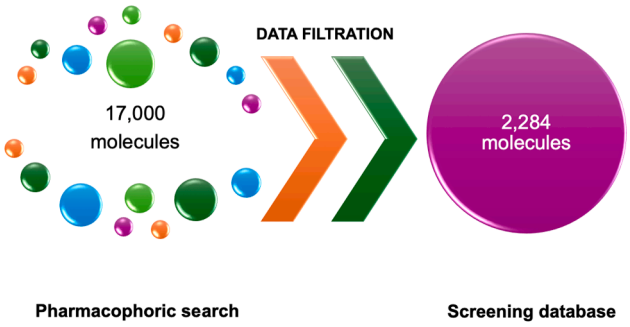

Fig. 3. Schematic representation of the number of molecules reduced after data filtration.

s://pharmit.csb.pitt.edu) [26]. Pharmit provides access to pre-built chemical libraries derived from central databases, including CHEMBL21 (over 1.4 million compounds), ChemDiv (over 1.4 million compounds), MolPort (over 6.5 million compounds), the NCI Open Chemical Repository (over 108,000 compounds), ZINC (over 13 million compounds), and PubChem (over 66 million compounds). These extensive datasets were utilized to perform pharmacophore-driven searches aimed at identifying novel candidate molecules. The screening process was carried out in "Pharmacophoric search" mode in three sequential steps. Initially, a pharmacophore model was generated that captured all the critical features of MRTX1133, with particular emphasis on the protonated nitrogen atom within the bridged ring, which forms a key salt bridge interaction with the mutant Asp12 residue (Fig. 2). This salt bridge is a crucial interaction for high-affinity binding and selectivity towards the KRAS G12D mutant, making it a focal point of the pharmacophore model. In subsequent rounds, the pharmacophore was progressively simplified by removing less critical features, thereby broadening the search criteria. The final models retained only essential elements such as the presence of a central aromatic ring, a positively charged nitrogen atom, and at least one hydrogen bond donor or acceptor. This stepwise relaxation of the pharmacophore constraints strikes a balance between specificity and sensitivity, enabling the identification of both close analogs and structurally novel scaffolds that maintain key interaction motifs. Hits retrieved from the pharmacophore searches were subjected to energy minimization and sorted based on binding affinity (e.g., affinities better than −7 kcal/mol) and minimum root-mean-square deviation (mRMSD) from the query pose, with a cutoff of 2 Å to eliminate poses with unfavorable geometries or significant conformational deviations. This filtering ensures that only energetically favorable and geometrically plausible candidates advance to subsequent docking and simulation steps.

Compounds from each library were downloaded in SDF format and subsequently merged into a unified database comprising approximately 17,000 molecules.

3.2. *Data filtering, ligand, and protein preparation*

The newly generated database contained several duplicate entries and compounds that did not meet established drug-likeness criteria. Therefore, a careful data curation step was essential to streamline the dataset and focus on molecules with more favorable pharmacokinetic and safety profiles. This refinement process ensures the reliability and quality of the dataset, which is critical for the success of subsequent virtual screening and docking studies. Refinement on the unified database was performed using DataWarrior software [22]. Initially, duplicate structures were identified and removed to ensure the uniqueness of the chemical entries. Subsequently, molecules flagged as potentially toxic, mutagenic, or reactive were systematically excluded to provide a safer chemical space for downstream analysis. This filtering reduces the risk of false positives and improves the translational potential of the identified hits. Physicochemical properties - including molecular weight (MW), partition coefficient (logP), and topological polar surface area (TPSA) - were then evaluated. Molecules were filtered according to the Lipinski Rule of Five (Ro5) [27] to prioritize candidates with favorable drug-like characteristics. Following all filtering steps, the final curated database comprised 2284 unique molecules, which were subsequently prepared for molecular docking by assigning appropriate protonation states and generating their three-dimensional structures (Fig. 3). The three-dimensional (3D) molecular structures of the compounds were generated using Open Babel (https://openbabel.org/index.html). All compounds were protonated at physiological pH (7.4), and energy minimization was conducted using the MMFF94s force field to optimize geometry and relieve steric clashes. Additionally, the lowest-energy conformer was generated for each molecule, ensuring that the docking simulations start from the most energetically favorable ligand conformations.

For the protein model, the KRAS G12D structure in complex with MRTX1133 ligand (PDB ID: 7RPZ) was retrieved from the Protein Data Bank using YASARA software [21]. The Homo sapiens structure, deposited on August 5, 2021, was resolved by X-ray diffraction at a high resolution of 1.30 Å and comprises 170 amino acids in chain A. The structure exhibits R-work = 0.149 and R-free = 0.171, indicating a high-quality fit to the experimental data. This structure was used as the starting model for molecular docking studies. Before docking, all non-essential elements, including co-crystallized ligands, water

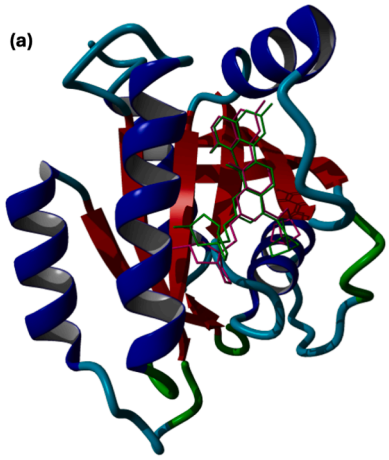

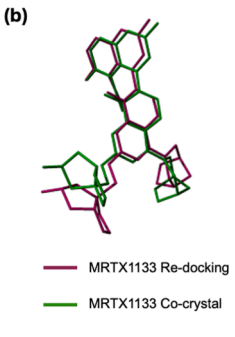

	ΔG VINA	CNN score	CNN affinity	K_i (nm)	pk_i
MRTX1133 Re-docking	-12.48	0.8509	8.615	1.576	8.803

Fig. 4. (a) Representation of 7RPZ structure in complex with MRTX1133 (co-crystallized and re-docking structures); (b) superimposition of MRTX1133 co-crystallized (green) and re-docked (violet) structures, with reported GNINA docking results.

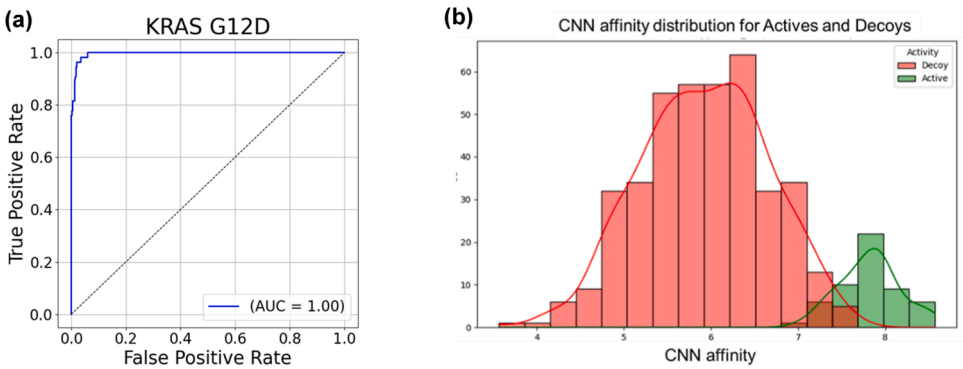

Fig. 5. (a) Receiver Operating Characteristic (ROC) curve for the CNN-based VS model targeting KRAS G12D. The AUC of 1.00 indicates perfect classification performance between active and inactive compounds. (b) Distribution of CNN prediction scores for actives (green) and decoys (red) in the KRAS G12D dataset. The score distribution reveals a distinct separation, with active compounds concentrated in the higher-scoring range, indicating the model's discriminative power.

molecules, and metal ions, were carefully removed to eliminate potential interference with ligand binding. The protonated structure was then subjected to energy minimization using the ff14SB force field, allowing for the relaxation of side chains and backbone conformations to resolve potential clashes or steric strain. This step helps obtain a more realistic and energetically favorable protein conformation, which can enhance docking accuracy. The binding site, corresponding to the switch II pocket, was defined around the coordinates of the original co-crystallized ligand (MRTX1133) and used to generate the docking box for subsequent simulations.

3.3. Docking validation and screening with GNINA

Before performing large-scale VS, GNINA [15,16], a machine learning-enhanced molecular docking platform, was validated to ensure its suitability for the KRAS G12D system. The validation step consisted of re-docking the co-crystallized ligand MRTX1133 into its binding site in the KRAS G12D structure (PDB ID: 7RPZ). The RMSD between the experimental and predicted binding poses was calculated to assess the accuracy of GNINA's docking predictions.

For the validation analysis, a *redocking* GNINA script was employed, generating nine binding poses per ligand, which were ranked in order of decreasing CNN score values. The best-scoring pose exhibited a root-mean-square deviation (RMSD) of 1.523 Å (calculated via DockRMSD v. 1.1) from the co-crystallized ligand, supporting the reliability and predictive accuracy of the docking protocol [28] (Fig. 4).

Furthermore, to comprehensively evaluate the performance of the VS protocol, we employed both early recognition metrics and global classification indicators. Specifically, we assessed the Receiver Operating Characteristic (ROC) curve. We calculated the Area Under the ROC Curve (AUC), which is a widely accepted tool for evaluating the discriminative capacity of binary classifiers [29]. As shown in Fig. 5, the ROC curve of the CNN-based model (GNINA) for KRAS G12D displays a near-perfect shape, with an AUC value of 1.00, indicating flawless classification between active and inactive compounds within the dataset. In addition to global performance, early recognition was quantitatively assessed using Enrichment Factors (EF) at various thresholds. The model yielded EF 1 % = 51.00, EF 5 % = 20.40, and EF 10 % = 10.20, highlighting its strong ability to rank active ligands within the top-scoring fraction of screened molecules. The remarkably high EF 1 % underscores the protocol's robustness in prioritizing true positives at the very early stage of the ranking, which is critical for cost-effective lead identification [30].

Taken together, these results provide strong evidence of the reliability and effectiveness of the GNINA-powered VS pipeline in identifying potential KRAS G12D binders. The combination of a perfect AUC and high EF values validates the predictive power of the method and supports its application in prospective drug discovery efforts.

Following successful validation, a two-step screening workflow was implemented. In the first step, the entire prepared database of 2284

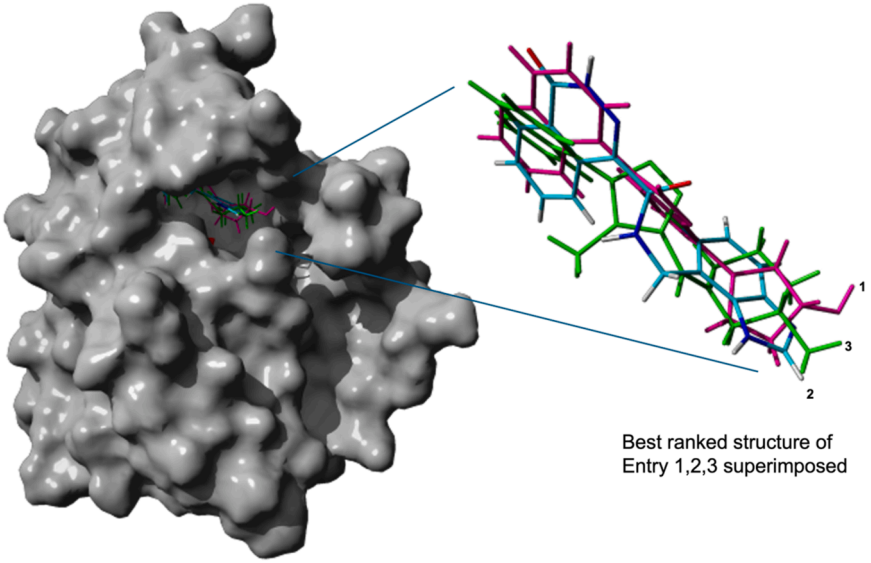

Fig. 6. Best-ranked pose of molecules 1–3 superimposed into the binding site of MRTX1133 in 7RPZ.

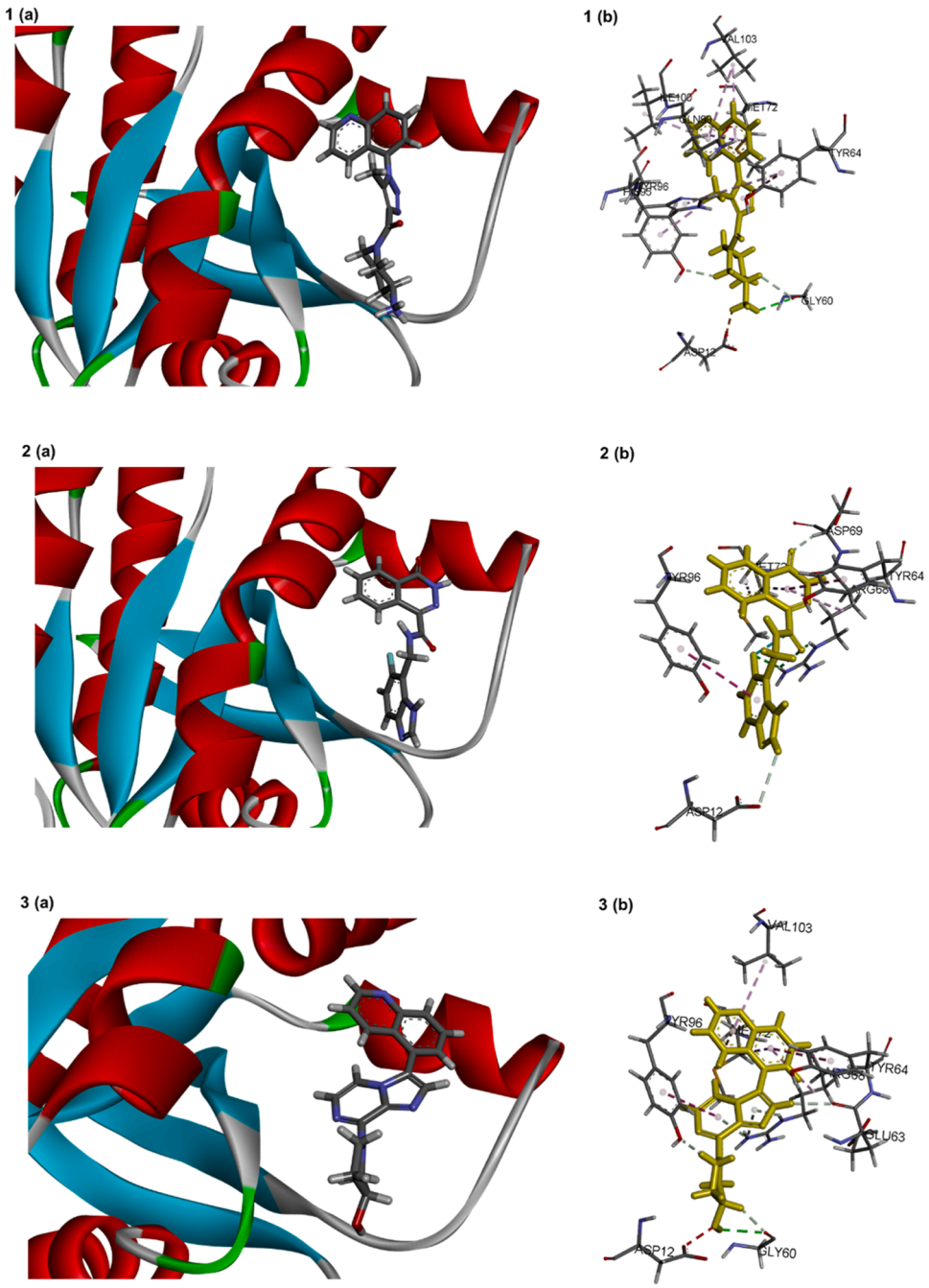

Fig. 7. (a) Illustration of the 3D complex of the compounds 1–3 within the KRAS G12D binding pocket; (b) detailed view of the interactions between the compound and the amino acid residues of the protein binding site.

compounds was subjected to a *rescoring* protocol in GNINA. This method rapidly evaluates binding affinities by combining the classical Vina scoring function with deep learning-derived Convolutional Neural Network (CNN) affinity predictions, ranking each pose based on both the predicted binding affinity (CNN score) and the CNN affinity. GNINA outputs were systematically tabulated and analyzed. Docking results were ranked based on predicted binding affinities, expressed as pK values (calculated from Vina ΔG using the equation $pK = -\Delta G/1.363$), along with CNN affinity scores. Molecules exhibiting both pK values and CNN scores greater than 6.3 were retained for further evaluation. This dual-filtering approach ensured a focus on compounds with consistent performance across both traditional and machine learning-based scoring, as demonstrated by us [31]. After applying these criteria, only 22 compounds passed the threshold and were selected for the next phase of the workflow (Table S1).

In the second step, the subset of pre-filtered molecules was subjected to a more rigorous docking protocol using GNINA's *refinement* mode, which enables enhanced pose sampling and local optimization to improve the accuracy of predicted ligand-receptor interactions [15]. The resulting docking poses were evaluated using the same criteria as the initial screening, but with more stringent cutoffs: only compounds with both predicted pK values and CNN affinity values greater than 6.5 were retained for further analysis. Following this refined filtering, 12 molecules met the updated thresholds. Notably, among these, only 3 compounds displayed pK values exceeding 7, suggesting stronger predicted binding affinity and marking them as top candidates for downstream MD evaluation (Figs. 6 and 7, Table 1).

Table 1
Structures and predicted CNN affinity and Vina pK values of best-ranked molecules after GNINA refinement and data evaluation.

Entry	Structure	SMILE	CNN affinity	Vina pK
1. CHEMBL4968507	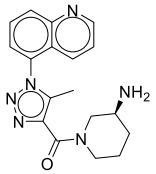	Cc1c(C(N(CCC2)C[C@H]2 N)=O)nn[n]1-c1cccc2ncccc12	7.08	7.79
2. Z4499936471	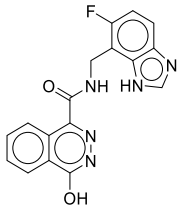	Oc1nnc(C(NCc(c2c(cc3)nc[nH]2)c3F)=O)c2ccccc12	6.81	7.53
3. MCULE-3539542683	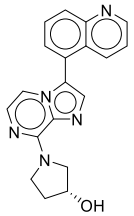	O[C@H](CC1)CN1c1ncc[n]2c1ncc2-c1cccc2ncccc12	6.59	7.44

3.4. Interaction analysis and binding mode comparison

The three top-ranked compounds identified through GNINA VS and filtering exhibit distinct, pharmacologically relevant structural features. All belong to heterocyclic scaffolds enriched with functional groups capable of establishing key molecular interactions within the KRAS G12D binding site. Their drug-like properties comply with Lipinski's Ro5, and their structural diversity offers multiple strategies for effective engagement of the mutant KRAS target. Compound **1** (CHEMBL4968507) is a triazole-chinoline derivative characterized by a moderately flexible scaffold, a terminal amide, and a chiral center. Its protonated amine forms a crucial electrostatic interaction, interpreted as a salt bridge, with Asp12, the residue mutated in KRAS G12D (Fig. 8). This anchoring interaction is particularly relevant, as binding to Asp12 is considered essential for selective inhibition of the G12D mutant. The extended aromatic system enables π-π stacking interactions, while additional hydrogen bonds with residues, such as Gly60 and Glu62, further stabilize its binding in the switch II pocket.

Compound **2** (Z4499936471), also a triazole derivative, contains a fluorinated aromatic ring, a hydroxyl group, and an amide moiety, making it the most polar of the three. It does not directly engage with Asp12, but forms hydrogen bonds with polar residues, such as Arg68 and Asp69, and π-π stacking interactions with Tyr96 and Tyr64. These interactions indicate strong potential for alternative binding stabilization and suggest good solubility and membrane permeability. Notably, the incorporation of fluorine is well-documented to improve metabolic stability by stabilizing the C-F bond against oxidative degradation and enhancing membrane crossing through modulation of lipophilicity and pK_a of adjacent groups [32,33]. Such properties make Compound **2** a promising candidate for further optimization, especially in terms of pharmacokinetics.

Compound **3** (MCULE-3539542683) features a rigid, planar purine-like fused heterocyclic system. It includes multiple nitrogen atoms and a chiral hydroxyl group, which facilitates both π-stacking and hydrogen bonding. Additional interactions, such as a hydrogen bond with Gly60, π-alkyl and π-cation with Arg68, and π-π stacking interactions with Tyr96 and Tyr64, located in the KRAS switch II region, support its high binding affinity. The compound's planarity and nucleotide-like geometry make it particularly well-suited for binding in deep or aromatic-rich pockets. These structural characteristics may also favor selectivity by mimicking endogenous nucleotide interactions, potentially reducing off-target effects.

To contextualize these findings, MRTX1133, a benchmark KRAS G12D inhibitor, forms a robust salt bridge with Asp12 *via* its protonated piperazine moiety. It also engages in hydrogen bonding with Glu62 and hydrophobic interactions within the switch II pocket, contributing to its high potency and selectivity for the G12D mutant (Table 2) [18]. This comparison highlights conserved interaction motifs critical for effective KRAS G12D inhibition, providing a valuable framework for rational drug design based on these key binding features.

3.5. Pharmacokinetics profile

To further characterize the pharmacokinetic potential of the screened compounds, we employed the *Brain Or IntestinaL EstimateD permeation* method (BOILED-Egg model) from SwissADME (http://www.swissadme.ch) to predict passive gastrointestinal absorption (HIA), blood-brain barrier (BBB) permeability, and P-glycoprotein (P-gp) efflux [34]. This model offers a graphical and intuitive representation of a molecule's oral absorption and potential for central nervous system (CNS) exposure. In the comprehensive screening of 22 molecules subjected to *refinement* (Fig. 9a), the majority are located within the white elliptical region, indicating high predicted gastrointestinal absorption. This suggests that most compounds are likely to have favorable oral bioavailability, a crucial factor for achieving a systemic therapeutic effect. A smaller subset of compounds resides within the yellow central region, suggesting potential for BBB penetration. The classification into P-gp substrates (blue circles) and non-substrates (red circles) further refines predictions about CNS exposure. Compounds identified as P-gp substrates are likely to be actively effluxed out of the brain, potentially limiting CNS accumulation and side effects.

Zooming in on the top 3 lead candidates (Fig. 9b), we observe that compounds **1** and **2** fall within the white (HIA+) region, indicating good potential for oral absorption. In detail, compound **1** is marked with a blue circle, suggesting it is a P-gp substrate (PGP+), potentially subject to active efflux from the brain; Compound **2** is marked with a red circle,

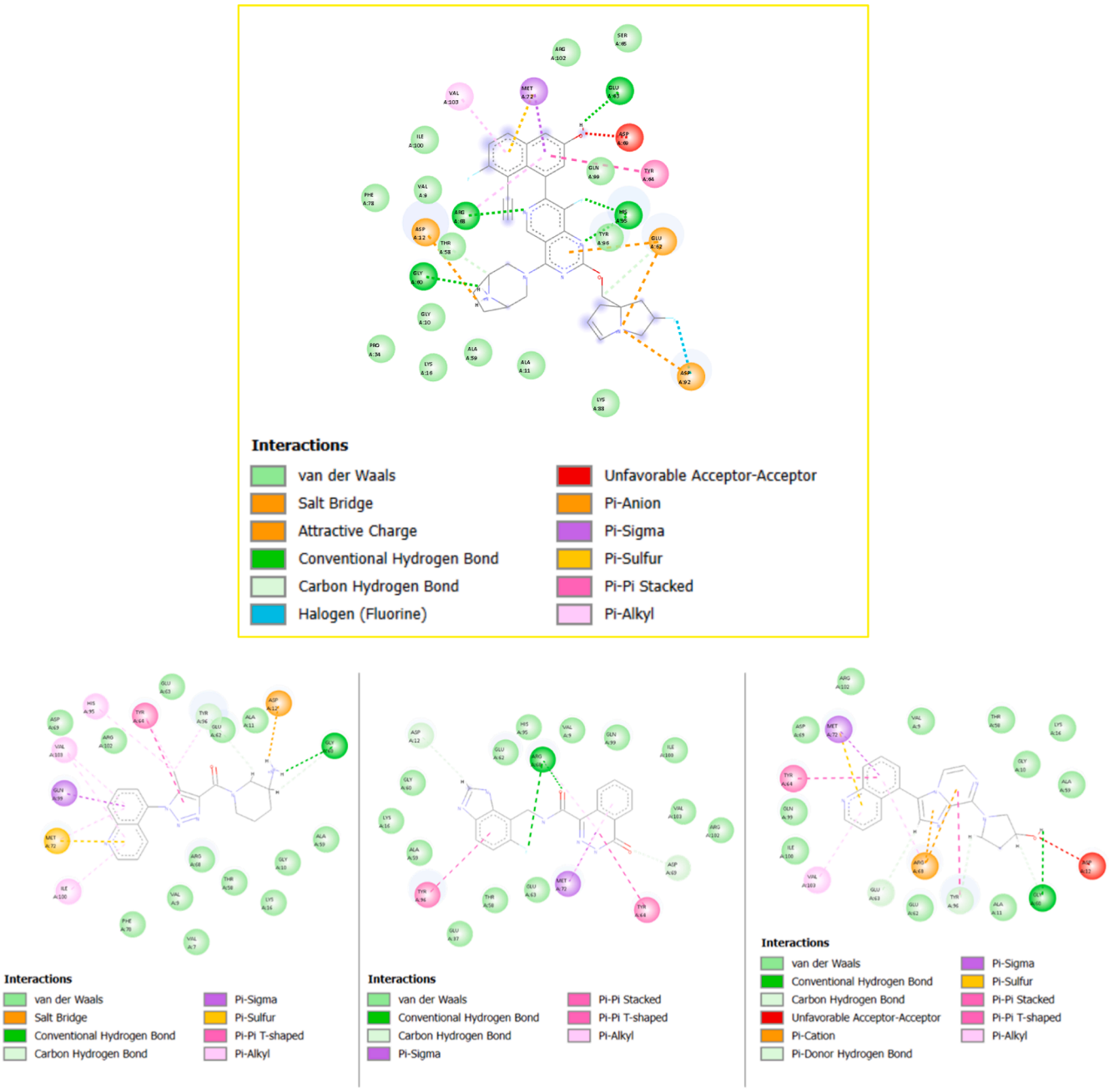

Fig. 8. 2D interaction diagrams of MRTX1133 from redocking (top), and compounds 1–3 (bottom, left to right) within the KRAS G12D binding pocket. The maps highlight specific contacts, such as hydrogen bonds, salt bridges, hydrophobic interactions, and π-π interactions, which are critical for stabilizing ligand binding.

indicating it is a P-gp non-substrate (PGP-), which may favor sustained systemic exposure. This profile enhances its potential as a peripheral therapeutic agent by improving bioavailability and reducing elimination. Compound **3**, however, lies within the yellow yolk, indicative of potential BBB penetration, and is marked as P-gp+, suggesting possible limited CNS accumulation due to efflux, despite its permeability.

This distribution suggests that compounds **1** and **2** are strong candidates for peripheral targets, with compound **2** having a slightly more favorable profile due to the lack of P-gp efflux. Compound **3** may exhibit CNS activity or have side effect potential and would require further profiling in this context.

3.6. Molecular dynamics and redocking

To validate the results obtained from molecular docking, 100 ns MD simulations were performed for the selected ligands (compounds **1**–**3**) against the 7RPZ protein target. The simulations were conducted using the YASARA software, employing the *md_runfast.mcr* macro to streamline the simulation process. This approach ensures a comprehensive and dynamic evaluation of ligand-protein interactions, extending beyond static docking snapshots to capture realistic molecular flexibility and solvent effects under physiologically relevant conditions. The stability of each ligand-protein complex was evaluated by analyzing fluctuations in potential energy (Fig. 9) and RMSD over time (Fig. 10). Between 60 and 100 ns, all ligands reached a stable conformation, as indicated by constant oscillations around an average value. This plateau suggests that the complexes had equilibrated, reflecting persistent binding conformations over the simulation timeframe. Such stability corroborates the docking predictions and indicates favorable binding under physiological-like conditions. The stability of the ligand-protein complexes was at first

Table 2
Comparison of key interactions of the three compounds and MRTX1133.

Residue	Compound 1	Compound 2	Compound 3	MRTX1133
Asp12	Salt bridge	H-bond	Unfavorable	Salt bridge
Glu62	H-bond	None	None	H-bond
Gly60	H-bond	None	H-bond	H-bond
His95	π-alkyl	None	None	H-bond
Tyr96	π-alkyl	π-π stacking	π-π stacking	H-bond
Asp92	None	None	None	Salt bridge, Halogen bond
Arg68	None	H-bond	π-Alkyl, π-Cation	π-alkyl, H-bond
Glu63	None	None	H-bond	H-bond
Met72	π-alkyl, π-sulfur	π-sigma	π-sigma, π-sulfur	π-sigma, π-sulfur
Tyr64	π-π stacking	π-π stacking	π-π stacking	π-π stacking
Asp69	None	H-bond	None	Unfavorable
Val103	π-alkyl	None	π-alkyl	π-alkyl

evaluated by monitoring potential energy and RMSD over the last 40 ns of the simulations. All three docked hits, as well as the co-crystallized ligand MRTX1133, reached equilibrated states characterized by stable energy profiles and convergent RMSD values (Figs 10, 11, and S1). The co-crystallized ligand displayed minimal fluctuations in both potential energy and RMSD, confirming the robustness of the simulation protocol and serving as a reliable benchmark. Compounds **1**–**3** exhibited highly comparable behavior, with their energy trajectories stabilizing around constant average values. The RMSD plots indicated restricted deviations within a range of ~1.2–1.8 Å for backbone atoms, consistent with stable binding conformations. Notably, Compound **3** showed slightly higher RMSD variability in the loop regions, though this remained within physiologically acceptable ranges.

To further analyze the stability of ligand-protein interactions, the average protein structure within the 60–100 ns window was calculated for each simulation using the *md_analyze* macro integrated within YASARA. Following the calculation of these average structures, the simulation box was regenerated to account for any necessary adjustments in the system's spatial configuration. This step refines the model by averaging out transient fluctuations, providing a representative snapshot of the complex at equilibrium suitable for subsequent redocking studies. The optimized ligands were then subjected to redocking using the *refinement* option of GNINA at the semiempirical level (Table 3). Visual inspection of the MD simulation trajectories confirmed that all ligands remained stably bound within the protein's catalytic site, without dissociating or exhibiting any significant conformational changes. This observation further validates the accuracy and reliability of the initial molecular docking predictions, reinforcing confidence in the predicted binding modes and suggesting strong and sustained ligand engagement with the target site.

3.7. PCA of KRAS G12D systems

To gain further insights into the collective motions and

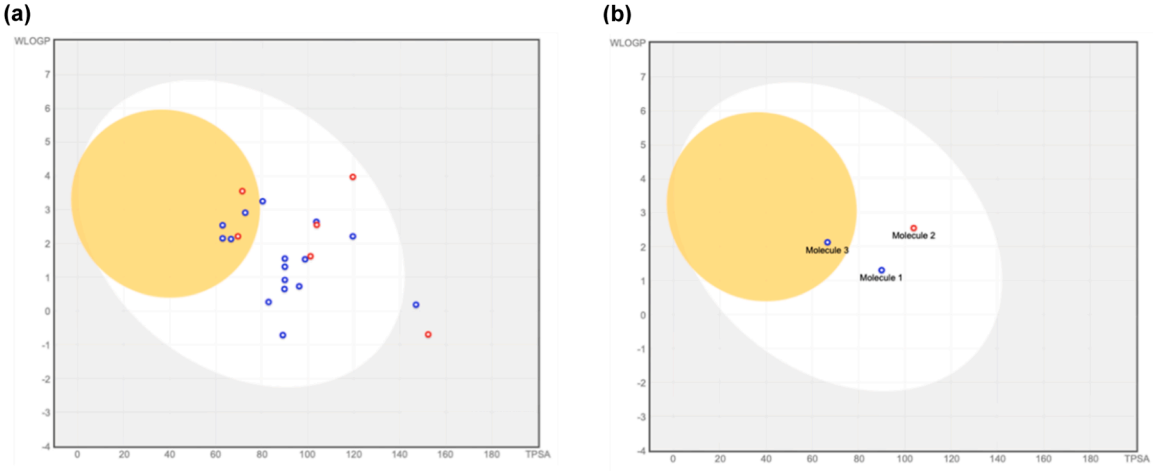

Fig. 9. (a) BOILED-Egg plot of all 22 refinement screened molecules. The white ellipse denotes high predicted passive gastrointestinal absorption (HIA+), while the yellow region represents molecules predicted to cross the blood-brain barrier (BBB+). Blue circles: predicted P-glycoprotein substrates (PGP+); red circles: non-substrates (PGP-). (b) BOILED-Egg plot of the top 3 lead compounds. Compounds 1 and 2 are located in the white region (HIA+), while compound 3 falls in the yellow yolk (BBB+). Compound 1 is PGP+, compound 2 is PGP-, and compound 3 is also PGP+.

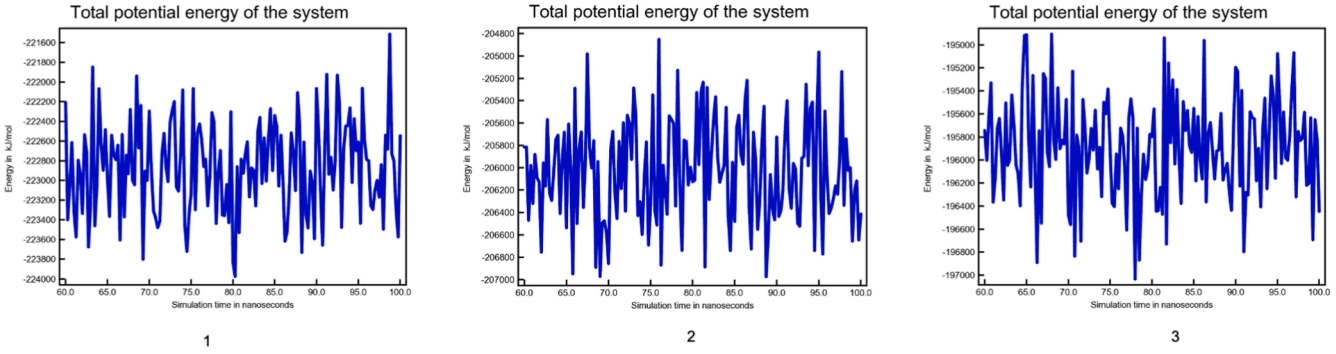

Fig. 10. Oscillations of total potential energy of the system (7RPZ protein + docked ligand) versus time retrieved from 60 to 100 ns MD simulation time window for compounds 1, 2, and 3.

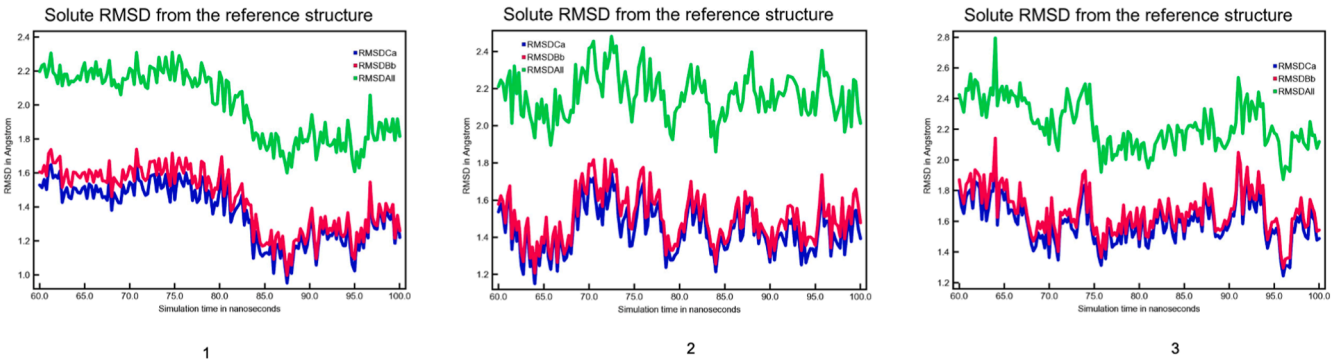

Fig. 11. Oscillations of potential energy versus time retrieved from 60 to 100 ns MD simulations time window for compounds 1, 2, and 3. The plot shows the RMSDs of alpha carbon (RMSDCa), backbone (RMSDBb), and all heavy atoms (RMSDAll).

Table 3
CNN affinity values obtained with GNINA refinement on the co-crystallized KRAS structure (pre-MD) and the average structure post-MD (60–100 ns).

Compound/Drug name	Before MD CNN affinity	Post MD CNN affinity
1/CHEMBL4968507	7.08	6.45
2/Z4499936471	6.80	5.26
3/MCULE-3539542683	6.59	6.19

conformational dynamics of KRAS G12D in both its apo form and in complex with inhibitors, PCA was performed. The eigenvalue (scree) plots (Fig. S2, left panels) highlighted the contribution of the first few principal components to the overall protein dynamics across all systems. The apo-KRAS G12D (Fig. S2a) displayed a higher proportion of variance captured by the first two components (40.6 % and 49.6 %) compared to the ligand-bound systems, suggesting enhanced intrinsic flexibility in the absence of inhibitors. Conversely, the KRAS G12D/MRTX1133 complex (Fig. S2b) exhibited a markedly steeper decline in eigenvalues, indicative of restricted global motions and enhanced stabilization induced by the inhibitor. A similar trend was observed for the KRAS G12D complexes with compounds **1**–**3** (Figs S2c-e), where the cumulative variance accounted for by the first two components was consistently lower than in the apo system, reflecting a reduction in conformational heterogeneity upon ligand binding.

The time-dependent projection of the trajectories onto the first two principal components (Fig. S2, center panels) further emphasized these differences. The apo system sampled a wider range of conformational states throughout the simulation, while the MRTX1133 and other inhibitor complexes displayed more localized and constrained distributions along the PC1 and PC2 axes. These findings indicate that the inhibitors effectively limit the conformational plasticity of KRAS G12D, stabilizing specific conformational substates.

The two-dimensional scatter plots of the trajectory projections onto PC1 and PC2 (Fig. S2, right panels) corroborated these observations. The apo system populated a broader conformational space with multiple subclusters, reflecting higher flexibility and diverse sampling of conformations. In contrast, the ligand-bound systems, particularly the KRAS G12D/**1** complex, exhibited a more compact and well-defined conformational landscape. The reduced dispersion of conformational states underscores the stabilizing role of ligand binding, which restricts large-scale fluctuations and locks the protein into fewer energetically favorable states.

Overall, the PCA analysis demonstrates that inhibitor binding, especially with compound **1**, significantly attenuates the dynamic motions of KRAS G12D, thereby reducing its conformational variability. These results, in agreement with RMSD analyses, reinforce the conclusion that ligand engagement stabilizes the protein structure, potentially enhancing binding efficacy and inhibitory potential.

4. Conclusions

In this study, we developed and validated a streamlined and integrated in silico workflow to identify potential inhibitors targeting the KRAS G12D switch-II pocket, one of the most elusive and therapeutically resistant sites in oncology. By combining pharmacophore-guided filtering, GNINA's machine learning-enhanced molecular docking, and molecular dynamics (MD) simulations, the workflow demonstrated a high level of efficiency and predictive accuracy while minimizing computational overhead.

The initial pharmacophore-based screening effectively narrowed the search space by prioritizing compounds with essential structural and functional features. Subsequent refinement through GNINA's CNN scoring significantly improved the reliability of hit identification, even in the face of KRAS G12D's notoriously shallow and dynamic binding site. Finally, molecular dynamics simulations offered critical insight into the conformational stability and binding persistence of selected ligands, strengthening confidence in their potential as viable inhibitors.

This multi-step, AI-augmented pipeline outperformed traditional virtual screening methods in terms of both speed and specificity, by focusing computational resources on a rigorously filtered compound set, a rational and resource-efficient drug repurposing strategy was facilitated, ultimately leading to the identification of three promising compounds with strong predicted affinity and stability within the KRAS G12D binding pocket.

Overall, the proposed workflow represents a powerful, time-saving alternative to conventional drug discovery pipelines. It underscores the value of integrating deep learning techniques with dynamic molecular simulations to accelerate the identification of therapeutics against high-priority yet difficult-to-drug oncogenic targets. These results pave the way for future experimental validation and broader application in precision oncology.

5. Ethics statement

The research presented in this manuscript does not require an Ethics Statement, as it does not involve any new experimentation with human or animal subjects. All analyses were conducted using simulated data derived from publicly available databases. No identifiable personal or sensitive information was used in this study. As such, no new ethical approval was required for the current computational and inferential analyses.

CRediT authorship contribution statement

Elisabetta Grazia Tomarchio: Writing – review & editing, Writing – original draft, Visualization, Validation, Methodology, Investigation, Formal analysis, Data curation. **Chiara Zagni:** Writing – review & editing, Writing – original draft, Investigation, Formal analysis, Data

curation. **Antonio Rescifina:** Writing – review & editing, Supervision, Resources, Project administration, Funding acquisition, Conceptualization.

Declaration of competing interest

The authors declare the following financial interests/personal relationships which may be considered as potential competing interests:

Antonio Rescifina reports that financial support was provided by PNRR MUR. If there are other authors, they declare that they have no known competing financial interests or personal relationships that could have appeared to influence the work reported in this paper.

Funding

Programma di ricerca CN00000013 “National Centre for HPC, Big Data and Quantum Computing”, finanziato dal Decreto Direttoriale di concessione del finanziamento n. 1031 del 17.06.2022 a valere sulle risorse del PNRR MUR - M4C2 - Investimento 1.4 - Avviso“Centri Nazionali” - D.D. n. 3138 del 16 dicembre 2021.

Supplementary materials

Supplementary material associated with this article can be found, in the online version, at doi:10.1016/j.insi.2025.100099.

Data availability

No data was used for the research described in the article.

References

[1] Prior IA, Hood FE, Hartley JL. The frequency of ras mutations in cancer. Cancer Res 2020;80:2969–74. https://doi.org/10.1158/0008-5472.CAN-19-3682.
[2] Zeissig MN, Ashwood LM, Kondrashova O, Sutherland KD. Next batter up! Targeting cancers with KRAS-G12D mutations. Trends Cancer 2023;9:955–67. https://doi.org/10.1016/j.trecan.2023.07.010.
[3] Kale R, Samant C, Nandakumar K, Ranganath Pai KS, Bhonde M. Drugging the Undruggable and beyond: emerging precision oncology approaches to target acquired resistance to KRAS G12C and KRAS G12D inhibitors. Biochem Biophys Res Commun 2025;760:151688. https://doi.org/10.1016/j.bbrc.2025.151688.
[4] Zheng Q, Peacock DM, Shokat KM. Drugging the Next Undruggable KRAS Allele-Gly12Asp. J Med Chem 2022;65:3119–22. https://doi.org/10.1021/acs.jmedchem.2c00099.
[5] Hunter JC, Manandhar A, Carrasco MA, Gurbani D, Gondi S, Westover KD. Biochemical and structural analysis of common cancer-associated KRAS mutations. Mol Cancer Res 2015;13:1325–35. https://doi.org/10.1158/1541-7786.MCR-15-0203.
[6] Moore AR, Rosenberg SC, McCormick F, Malek S. RAS-targeted therapies: is the undruggable drugged? Nat Rev Drug Discov 2020;19:533–52. https://doi.org/10.1038/s41573-020-0068-6.
[7] Canon J, Rex K, Saiki AY, Mohr C, Cooke K, Bagal D, Gaida K, Holt T, Knutson CG, Koppada N, Lanman BA, Werner J, Rapaport AS, San Miguel T, Ortiz R, Osgood T, Sun J-R, Zhu X, McCarter JD, Volak LP, Houk BE, Fakih MG, O’Neil BH, Price TJ, Falchook GS, Desai J, Kuo J, Govindan R, Hong DS, Ouyang W, Henary H, Arvedson T, Cee VJ, Lipford JR. The clinical KRAS(G12C) inhibitor AMG 510 drives anti-tumour immunity. Nature 2019;575:217–23. https://doi.org/10.1038/s41586-019-1694-1.
[8] Hallin J, Engstrom LD, Hargis L, Calinisan A, Aranda R, Briere DM, Sudhakar N, Bowcut V, Baer BR, Ballard JA, Burkard MR, Fell JB, Fischer JP, Vigers GP, Xue Y, Gatto S, Fernandez-Banet J, Pavlicek A, Velastagui K, Chao RC, Barton J, Pierobon M, Baldelli E, Patricoin EF, Cassidy DP, Marx MA, Rybkin II, Johnson ML, Ou S-HI, Lito P, Papadopoulos KP, Jänne PA, Olson P, Christensen JG. The KRASG12C inhibitor MRTX849 provides insight toward therapeutic susceptibility of KRAS-mutant cancers in mouse models and patients. Cancer Discov 2020;10:54–71. https://doi.org/10.1158/2159-8290.CD-19-1167.
[9] Mottini C, Tomihara H, Carrella D, Lamolinara A, Iezzi M, Huang JK, Amoreo CA, Buglioni S, Manni I, Robinson FS, Minelli R, Kang Y, Fleming JB, Kim MP, Bristow CA, Trisciuoglio D, Iuliano A, Del Bufalo D, Di Bernardo D, Melisi D, Draetta GF, Ciliberto G, Carugo A, Cardone L. Predictive signatures inform the effective repurposing of decitabine to treat KRAS-dependent pancreatic ductal adenocarcinoma. Cancer Res 2019;79:5612–25. https://doi.org/10.1158/0008-5472.CAN-19-0187.
[10] Tripathi P, Soni R, Antra, Tandon V. Pixantrone confers radiosensitization in KRAS mutated cancer cells by suppression of radiation-induced prosurvival pathways. Free Radic Biol Med 2022;190:351–62. https://doi.org/10.1016/j.freeradbiomed.2022.08.015.
[11] Ancy I, Penislusshiyan S, Ameen F, Chitra L. Microsecond molecular dynamics simulation to gain insight into the binding of MRTX1133 and trametinib with $KRAS^{G12D}$ mutant protein for drug repurposing. J Mol Recognit 2024;37:e3103. https://doi.org/10.1002/jmr.3103.
[12] Singhal S, Mehta J, Desikan R, Ayers D, Roberson P, Eddlemon P, Munshi N, Anaissie E, Wilson C, Dhodapkar M, Zeldis J, Siegel D, Crowley J, Barlogie B. Antitumor activity of thalidomide in refractory multiple myeloma. N Engl J Med 1999;341:1565–71. https://doi.org/10.1056/NEJM199911183412102.
[13] Huang M, Ye Y, Chen S, Chai J, Lu J, Zhoa L, Gu L, Wang Z. Use of all-trans retinoic acid in the treatment of acute promyelocytic leukemia. Blood 1988;72:567–72. https://doi.org/10.1182/blood.V72.2.567.567.
[14] Vogel VG. Effects of tamoxifen vs raloxifene on the risk of developing invasive breast cancer and other disease outcomesThe NSABP study of tamoxifen and raloxifene (STAR) P-2 Trial. JAMA 2006;295:2727. https://doi.org/10.1001/jama.295.23.joc60074.
[15] McNutt AT, Francoeur P, Aggarwal R, Masuda T, Meli R, Ragoza M, Sunseri J, Koes DR. GNINA 1.0: molecular docking with deep learning. J Cheminform 2021;13:43. https://doi.org/10.1186/s13321-021-00522-2.
[16] McNutt AT, Li Y, Meli R, Aggarwal R, Koes DR. GNINA 1.3: the next increment in molecular docking with deep learning. J Cheminform 2025;17:28. https://doi.org/10.1186/s13321-025-00973-x.
[17] Francoeur PG, Masuda T, Sunseri J, Jia A, Iovanisci RB, Snyder I, Koes DR. Three-dimensional convolutional neural networks and a cross-docked data set for structure-based drug design. J Chem Inf Model 2020;60:4200–15. https://doi.org/10.1021/acs.jcim.0c00411.
[18] Wang X, Allen S, Blake JF, Bowcut V, Briere DM, Calinisan A, Dahlke JR, Fell JB, Fischer JP, Gunn RJ, Hallin J, Laguer J, Lawson JD, Medwid J, Newhouse B, Nguyen P, O’Leary JM, Olson P, Pajk S, Rahbaek L, Rodriguez M, Smith CR, Tang TP, Thomas NC, Vanderpool D, Vigers GP, Christensen JG, Marx MA. Identification of MRTX1133, a Noncovalent, Potent, and Selective $KRAS^{G12D}$ Inhibitor. J Med Chem 2022;65:3123–33. https://doi.org/10.1021/acs.jmedchem.1c01688.
[19] Hallin J, Bowcut V, Calinisan A, Briere DM, Hargis L, Engstrom LD, Laguer J, Medwid J, Vanderpool D, Lifset E, Trinh D, Hoffman N, Wang X, David Lawson J, Gunn RJ, Smith CR, Thomas NC, Martinson M, Bergstrom A, Sullivan F, Bouhana K, Winski S, He L, Fernandez-Banet J, Pavlicek A, Haling JR, Rahbaek L, Marx MA, Olson P, Christensen JG. Anti-tumor efficacy of a potent and selective non-covalent KRASG12D inhibitor. Nat Med 2022;28:2171–82. https://doi.org/10.1038/s41591-022-02007-7.
[20] R.J. Gunn, N.C. Thomas, W. Xiaolun, J.D. Lawson, M.A. Marx, KRAS G12D in complex with MRTX-1133: 7rpz, (2021). https://doi.org/10.2210/pdb7rpz/pdb.
[21] Krieger E, Vriend G. YASARA View—Molecular graphics for all devices—from smartphones to workstations. Bioinformatics 2014;30:2981–2. https://doi.org/10.1093/bioinformatics/btu426.
[22] Sander T, Freyss J, Von Korff M, Rufener C. DataWarrior: an open-source program for chemistry aware data visualization and analysis. J Chem Inf Model 2015;55:460–73. https://doi.org/10.1021/ci500588j.
[23] Sharma A, Noda M, Sugiyama M, Ahmad A, Kaur B. Production of functional buttermilk and soymilk using pediococcus acidilactici BD16 (alaD+). Molecules 2021;26:4671. https://doi.org/10.3390/molecules26154671.
[24] Liu T, Lin Y, Wen X, Jorissen RN, Gilson MK. BindingDB: a web-accessible database of experimentally determined protein-ligand binding affinities. Nucleic Acids Res 2007;35:D198–201. https://doi.org/10.1093/nar/gkl999.
[25] Güner OF, Bowen JP. Setting the record straight: the origin of the pharmacophore concept. J Chem Inf Model 2014;54:1269–83. https://doi.org/10.1021/ci5000533.
[26] Sunseri J, Koes DR. Pharmit: interactive exploration of chemical space. Nucleic Acids Res 2016;44:W442–8. https://doi.org/10.1093/nar/gkw287.
[27] Lipinski CA, Lombardo F, Dominy BW, Feeney PJ. Experimental and computational approaches to estimate solubility and permeability in drug discovery and development settings. Adv Drug Deliv Rev 1997;23:3–25. https://doi.org/10.1016/S0169-409X(96)00423-1.
[28] Ramírez D, Caballero J. Is it reliable to take the molecular docking top scoring position as the best solution without considering available structural data? Molecules 2018;23:1038. https://doi.org/10.3390/molecules23051038.
[29] Truchon J-F, Bayly CI. Evaluating Virtual Screening Methods: good and Bad Metrics for the “Early Recognition” Problem. J Chem Inf Model 2007;47:488–508. https://doi.org/10.1021/ci600426e.
[30] Li J, Liu W, Song Y, Xia J. Improved method of structure-based virtual screening based on ensemble learning. RSC Adv 2020;10:7609–18. https://doi.org/10.1039/C9RA09211K.
[31] Buccheri R, Rescifina A. High-Throughput, High-Quality: benchmarking GNINA and AutoDock Vina for precision virtual screening workflow. Molecules 2025;30:3361. https://doi.org/10.3390/molecules30163361.
[32] Shabir G, Saeed A, Zahid W, Naseer F, Riaz Z, Khalil N, Muneeba, Albericio F. Chemistry and pharmacology of fluorinated drugs approved by the FDA (2016-2022). Pharmaceuticals 2023;16:1162. https://doi.org/10.3390/ph16081162.
[33] Shah P, Westwell AD. The role of fluorine in medicinal chemistry: review Article. J Enzyme Inhib Med Chem 2007;22:527–40. https://doi.org/10.1080/14756360701425014.
[34] Daina A, Zoete V. A BOILED-egg to predict gastrointestinal absorption and brain penetration of small molecules. ChemMedChem 2016;11:1117–21. https://doi.org/10.1002/cmdc.201600182.